PROCEEDINGS OF SPIE

SPIEDigitalLibrary.org/conference-proceedings-of-spie

Highly uniform 150 mm diameter multichroic polarimeter array deployed for CMB detection

Ho, Shuay-Pwu Patty, Austermann, Jason, Beall, James, Choi, Steve, Cothard, Nicholas, et al.

Shuay-Pwu Patty Ho, Jason Austermann, James A. Beall, Steve K. Choi, Nicholas F. Cothard, Kevin T. Crowley, Rahul Datta, Mark J. Devlin, Shannon M. Duff, Patricio A. Gallardo, Matthew Hasselfield, Shawn W. Henderson, Gene Hilton, Johannes Hubmayr, Brian J. Koopman, Yaqiong Li, Jeffrey McMahon, Michael D. Niemack, Maria Salatino, Sara M. Simon, Suzanne T. Staggs, Jonathan T. Ward, Joel N. Ullom, Eve M. Vavagiakis, Edward J. Wollack, "Highly uniform 150 mm diameter multichroic polarimeter array deployed for CMB detection," Proc. SPIE 9914, Millimeter, Submillimeter, and Far-Infrared Detectors and Instrumentation for Astronomy VIII, 991418 (7 March 2017); doi: 10.1117/12.2233113

SPIE.

Event: SPIE Astronomical Telescopes + Instrumentation, 2016, Edinburgh, United Kingdom

Highly uniform 150 mm diameter multichroic polarimeter array deployed for CMB detection

Shuay-Pwu Patty Ho[a], Jason Austermann[b], James A. Beall[b], Steve K. Choi[a], Nicholas F. Cothard[d], Kevin Crowley[a], Rahul Datta[e], Mark J. Devlin[c], Shannon M. Duff[b], Patricio A. Gallardo[d], Matthew Hasselfield[g], Shawn W. Henderson[d], Gene Hilton[b], Johannes Hubmayr[b], Brian J. Koopman[d], Yaqiong Li[a], Jeffery McMahon[e], Michael D. Niemack[d], Maria Salatino[a], Sara M. Simon[e], Suzanne T. Staggs[a], Jonathan T. Ward[c], Joel N. Ullom[b], Eve M. Vavagiakis[d], and Edward J. Wollack[f]

[a]Princeton University, Princeton, NJ 08540, USA
[b]National Institute of Standards and Technology, Boulder, CO 80305, USA
[c]University of Pennsylvania, Philadelphia, PA 19104, USA
[d]Cornell University, Ithaca, NY 14850, USA
[e]University of Michigan, Ann Arbor, MI 48109, USA
[f]NASA Goddard Space Flight Center, Greenbelt, MD 20771, USA
[g]Pennsylvania State University, State College, PA 16801, USA

ABSTRACT

The Advanced Atacama Cosmology Telescope Polarimeter is an upgraded receiver for the Atacama Cosmology Telescope, which has begun making measurements of the small angular scale polarization anisotropies in the Cosmic Microwave Background using the first of four new multichroic superconducting detector arrays. Here, we review all details of the optimization and characterization of this first array, which features 2012 AlMn transition-edge sensor bolometers operating at 150 and 230 GHz. We present critical temperatures, thermal conductivities, saturation powers, time constants, and sensitivities for the array. The results show high uniformity across the 150 mm wafer and good performance in the field.

Keywords: Cosmic Microwave Background, Multichroic, Transition-Edge Sensor, Bolometer

1. INTRODUCTION

Over the past two decades improvements in low-temperature detector arrays have significantly advanced our knowledge of the cosmic microwave background (CMB) and sub-millimeter astronomy. To make further progress, increasing array detector counts is key to increasing total array sensitivities, if the detectors composing the arrays are background-limited. The largest detector arrays in development use transition-edge sensors (TES), presently the most mature superconducting detector technology, and have demonstrated near photon-noise dominated performance on current CMB instruments. Large TES arrays are achieving ever higher map sensitivities and mapping speeds, improvements which are advancing our knowledge of the history and structure of our Universe.

Advanced ACTPol, an upgrade to the ACTPol receiver on the Atacama Cosmology Telescope, is deploying some of the largest TES arrays yet produced in order to better characterize both the intensity and polarization of the CMB sky. The Atacama Cosmology Telescope (ACT) is located at an altitude of 5190 m in the Atacama Desert in northern Chile. ACT consists of a 6 m primary mirror and a 2 m secondary mirror in an off-axis Gregorian configuration. Since 2008, the ACT telescope has observed the temperature anisotropies of the CMB at millimeter wavelengths.[1] A polarization sensitive camera, ACTPol,[2] was deployed on ACT beginning in 2013, and precision first and second season measurements of CMB polarization were presented in Naess et al. 2014[3] and Louis et al. 2016.[4] The AdvACT upgrade will have four new feedhorn-coupled multichroic array packages

Further author information: (Send correspondence to S. P. Ho)
S. P. Ho: E-mail: spho@princeton.edu, Telephone: 1 609 712 0814

Millimeter, Submillimeter, and Far-Infrared Detectors and Instrumentation for Astronomy VIII,
edited by Wayne S. Holland, Jonas Zmuidzinas, Proc. of SPIE Vol. 9914, 991418
 · doi: 10.1117/12.2233113

sensitive in five frequency bands spanning from 28 GHz to 230 GHz, and plans to map approximately half of the sky.[5,6] AdvACT's increased optical frequency coverage over ACTPol, which observed only in bands centered at 90 and 150 GHz, will aid in the removal of synchrotron and dust foregrounds which obscure the CMB signal. In addition, AdvACT's arrays will be more sensitive to CMB temperature and polarization than ACTPol's by approximately a factor of two, achieved primarily by doubling the number of the detectors in the mid- and high-frequency arrays as detailed in Henderson et al. 2016.[5] The first AdvACT high-frequency (HF) multichroic detector array was built, characterized in the lab, and deployed on the ACT telescope in 2016, and is sensitive in bands centered at 150 and 230 GHz. Going forward, AdvACT plans to deploy two mid-frequency (MF) arrays sensitive in bands centered at 90 and 150 GHz in early 2017. In 2018 an additional low-frequency (LF) array, with sensitivity centered at 28 and 40 GHz, will replace one of the two MF arrays.

This paper reports the measured performance of the AdvACT HF array in both the laboratory and in the field. The HF array was fabricated on a single 150 mm-diameter silicon wafer[7] and has 503 optical pixels and 3 dark pixels for a total of 2024 detectors. In contrast to the ACTPol arrays, each of which was composed from as many as six individual 3″ wafers, this new monolithic array design allows for more efficient pixel packing, resulting in higher pixel densities in the ACT focal plane.[2] In Section 2, we discuss the HF detector array package. In Section 3.1 and 3.3, we present measurements of the HF array parameters, including detector critical temperatures (T_c), saturation powers (P_{sat}), thermal conductivities (G), and corner frequencies (f_{3dB}), as well as the total array sensitivity in both bands. In Section 3.2, we present multiple estimates of the on-site loading from the atmosphere and instrument in the field. We conclude in Section 4 with a discussion of the status and future plans for AdvACT.

2. HF ARRAY

The HF array package is shown in Figure 1. Signals from the sky pass through the receiver window, lenses and filters, and are coupled to feedhorns in a gold-plated silicon platelet feedhorn array. A wide band spline-profiled design was chosen for the feedhorns in order to optimize coupling efficiency, and each feedhorn defines the beam of an array pixel on the sky. Each feedhorn focuses detected radiation onto the antenna probes of an orthomode transducer on one of the array's pixels which separates the light into two polarizations. On-chip band defining filters then separate each polarization signal into the array's two frequency bands and feed the separated polarization and frequency signals onto one of the pixel's four TES islands for detection. The 150 mm detector wafer is in the center of the array package, and is attached to the feedhorn array by a clamping ring on the back of the array package. Readout electronics are housed on a 12″ PCB surrounding the array. The array package is coupled to the mixing chamber of a dilution refrigerator, which maintains a continuous operating bath temperature of ~ 100 mK in the field. Due to the larger detector wafer size, the shape and size of the HF detector array package is significantly different than the array packages deployed on ACTPol. Subsequently, substantial adjustments to array mounting hardware, magnetic shielding, and heat sinking were required to accomodate the HF array. This work afforded the opportunity for several improvements including the elimination of several unnecessary thermal joints in order to improve the heat sinking of the array.[8] In addition, we replaced all receiver optical elements (filters, anti-reflection coated silicon lenses,[9] and feedhorns) with wider bandwidth versions to match the bandwidth of the optical chain required for the multichroic HF array.[10]

2.1 HF detector array

The HF array has 506 feedhorn-coupled multichroic pixels with 2024 AlMn-based TESs fabricated on a single 150 mm, 500 μm thick silicon detector wafer. Each multichroic pixel has four bolometers, two for each linear polarization, for a total of 2024 detectors on the HF array.[7] The TESs are made of a single layer of aluminum manganese (AlMn) alloy, with a critical temperature of $T_c \sim 160$ mK. This target critical temperature was selected by optimizing the detector thermal sensitivity, which is related to the TES thermal properties and the operating bath temperature. An image of an AdvACT HF TES island is shown on the bottom right of Figure 2, with the AlMn alloy film located in the middle of the TES island. The use of a single layer of AlMn alloy simplifies the fabrication process and consistently gives improved measured device parameter uniformity across AdvACT's large 150 mm diameter wafers.[11] When operating the TES bolometers, the TESs are cooled below their critical temperature and voltage-biased onto their transition. Measured changes in the TES current are

then proportional to changes in the observed optical signal. It is necessary to maintain the cryostat at a 100 mK bath temperature continuously. The HF TES bolometers were designed to optimize their performance and noise properties under the expected bath and loading conditions in the field.

2.2 Readout

Each array TES has a pair of signalling lines connecting it into cryogenic readout circuitry which amplifies and routes the detector signals to warm electronics for digitization at 300 K. Signals from the array connect to the readout first through custom flexible superconducting cables (flex), consisting of aluminum traces on a flexible polymide substrate.[12] The flex cables connect signals from the array into large silicon wiring chips, which in turn route the array signals into smaller chips which implement the first stage of the cryogenic readout at 100 mK. The large silicon wiring chips have additional signal routing and bondpads to connect to readout control signals fed to the wiring chips (SQUID biases, SQUID feedbacks, and TES biases) through a large annular PCB which circumbscribes the array. The array is read out using a superconducting quantum interference device-based (SQUID) time-division multiplexing (TDM) scheme.[13,14] The multiplexed readout allows multiple SQUIDs to share common bias and feedback lines, which reduces the number of wires required to connect the 300 K ambient electronics to the coldest detector stage, thereby reducing the heat load on the cryogenics and allowing us to maintain base temperatures of 100 mK. The detectors are biased using shunt resistors, housed on interface chips, which also have inductors to band limit the TES response. The interface chips have three wirebond selectable inductance options, giving flexibility to allow for the optimization of the TES readout bandwidth. Informed by measurements of dark noise in test devices, for the HF array the bonding option was selected that added minimal inductance to the TES circuit. Due to differences in expected loading, detectors observing at different optical frequencies have different voltage bias lines, with multiple interface chips biased in series on each bias line. In the HF array, the detectors are grouped into 24 bias lines, each with 66, 88, or 110 TESs, depending on the location of the TESs in the array. The readout is described in more detail in Henderson et al. 2016.[15]

The SQUID multiplexing chips and interface chips are epoxied onto the wiring chips and grouped into readout units in an optimal way based on the results of extensive screening. In total, the HF array contains 304 large and small silicon chips and requires over 21,000 wire bonds for the readout of its 2024 TESs. Robust assembly is critical – for example, successful readout of one detector requires 55 successful superconducting wire bonds on average. We have successfully developed and demonstrated procedures for robust assembly on this HF array.[16] The fully assembled HF array is shown in Figure 1.

3. DETECTOR PERFORMANCE

The TES island is approximately an isothermal unit, with heat capacity C and temperature T_{TES}. Two sources of power are optical power from incident radiation absorbed by the TES island and bias power from the TES bias circuit. Heat leaves the island through a weak thermal link (the SiN legs) with thermal conductivity G to the bath. Figure 2 shows the 150 mm detector wafer, a single pixel with four TES islands, and a zoom-in on a TES island for the HF 150/230 GHz design. Shown in the bottom right of Figure 2, the TES island is linked to the bath by four SiN legs. One of four legs carries signal from the feedhorn on a transmission line that terminates in a lossy Au meander. Another leg carries the bias line which keeps the TES on its transition. The geometry and material properties of the legs define the thermal conductivity to the bath. A region of PdAu is added to the TES island to tune its heat capacity for electrothermal stability, and to tune the TES time response.[17–19] The detector performance is mainly described by three characteristics. One is the detector saturation power, P_{sat}, which determines the functionality of a detector during observation. The second one is the time constant, τ, which indicates how fast the detectors respond to a signal. The third one is the detector noise. Preliminary measurements with HF TESs in the field indicate that the sensors are photon noise dominated, and the TES phonon noise is sub-dominant to the noise associated with photon loading, which affects the sensitivity of the final sky map. The HF array parameters are summarized in table 1, along with the on-sky performance. The yield of the working TESs is over 70%. The 30% loss are majorly from the multiplexing and the voltage biasing

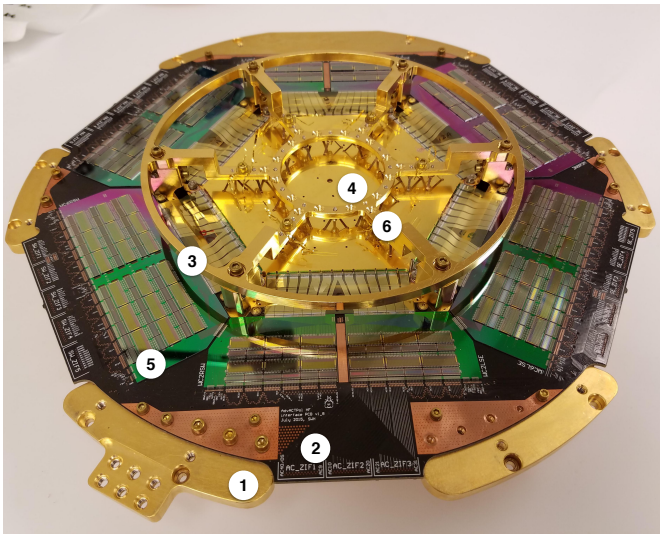

Figure 1: The HF array package shown from the non-sky side. (1) Copper ring, the PCB support. (2) The 12″ annular PCB. (3) The detector clamp ring, with 24 tripod springs attached, mechanically pressing the wafer in place on the non-skyside of the feedhorn array. (4) The detector wafer. All the signals are read out from six edges of the wafer through the flexes onto the PCB. (5) Readout chips; the large base chips are wiring chips; smaller chips are multiplexing chips and interface chips. (6) The label shows the position of the thermometer, which measures the HF temperature during laboratory measurements.

lines, $\sim 14\%$ and 11% respectively. We have identified the problems, which is due to the wire bonds on the readout chips and the repair work after laboratory testing. Improvements have been discussed in the future assembly, and we believe that the array yield will be highly improved after the experience learned from the HF array.

ν (GHz)	T_c (mK)	$P_{\rm sat}$ (pW)	G (pW/K)	n	f_{3dB} (Hz)	Array NET (μK$\sqrt{s}$)
150	165 ± 2	13 ± 1	371 ± 16	3.71 ± 0.01	78 ± 9	11
230	165 ± 3	26 ± 1	719 ± 21	3.83 ± 0.01	104 ± 12	21

Table 1: The measured median AdvACT HF detector parameter values. The first column indicates which frequency band is described subsequently. The array noise-equivalent temperature (NET) of AdvACT's detectors is estimated based on the time-stream noise at 20 Hz. All parameters shown here are measured in the laboratory without the optical loading from the optics tube used in the field camera; except for f_{3dB} and array NET, which are measured on the telescope with the planet method described in the text. The errors are the median absolute deviation of the detector distributions.

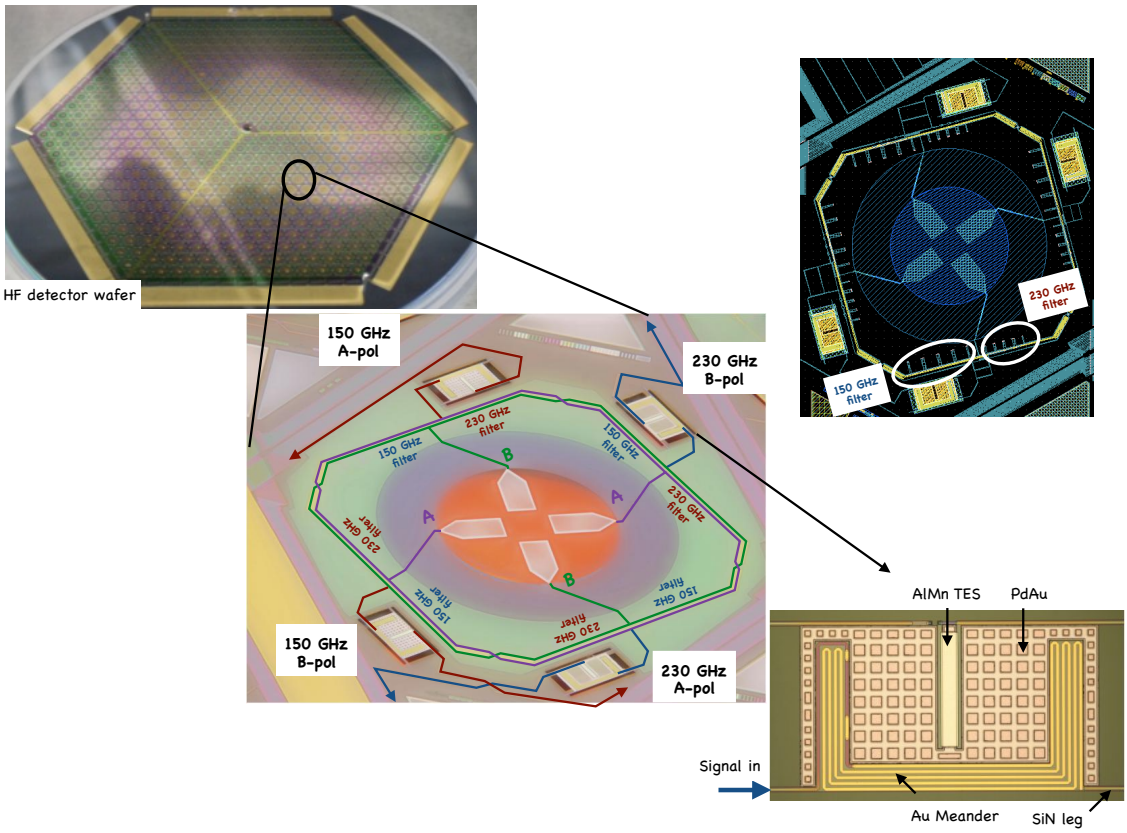

Figure 2: (Top left) The HF wafer, containing 506 pixels and 2024 TESs. The wiring on the wafer is routed to the six sides of the hexagon where electrical connections are made with aluminum wire bonds. (Middle) A single HF pixel. The incident radiation couples to the four TESs via the central antenna, whose four fins are optimized for a broad band response. These probes split the radiation into two orthogonal components, shown in purple and green lines. The light paths are drawn in blue and red lines. The signals are then split into the two frequency bands with a set of diplexing stub filters, which are best seen in the photo on the upper right. The specific frequency and polarization output is then absorbed by an ohmic Au meander on a TES island. (Bottom right) The TES island for the HF 150 GHz design. The island is connected to the bath through 4 SiN legs on the four corners. Signals come in through one SiN leg and terminate in the Au meander. A second leg carries the TES bias line pair which maintains the AlMn film in the center of the island on its transition. PdAu is added to the TES island to tune its heat capacity by changing its geometry and thickness.

3.1 Saturation Power

We define the detector saturation power P_{sat} as the electrical bias power required to drive the TES resistance to 90% of its normal resistance R_n. The HF array target P_{sat} at 100 mK bath is 12.5 pW for the 150 GHz band and 25 pW for the 230 GHz band. These P_{sat} values were chosen for optimum detector operation on the telescope, considering the operating bath temperature, atmospheric loading, and the expected detector efficiency. The designed transition temperature is 160 mK. Prior to deployment, we characterized these thermal and electrical properties on the HF array in the laboratory using a dilution refrigerator that is capable of providing a bath temperature less than 40 mK with the HF array package installed.

Bolometers register any additional power on the TES island, whether it is incident radiation or electrical power.

We use laboratory measurements to evaluate the saturation power of the detectors at various temperatures and predict saturation powers expected on the telescope Using a standard parameterization to determine the relationship between the bath temperature and the saturation power, we solve for the thermal conductivity, G, between the island and the bath,[20]

$$P_{sat} = \kappa(T_c^n - T_{bath}^n), \tag{1}$$

$$G = dP_{sat}/dT|_{T_c} = n\kappa T_c^{n-1}, \tag{2}$$

where the power law index n and thermal conductance κ are determined by the geometry and material properties of the TES legs, which provide a weak thermal link to the bath.

We voltage bias the detectors through the superconducting transition to acquire current-voltage (I-V) curves and measure P_{sat} at various bath temperatures. We then use Eq.(1) to estimate T_c, κ, and n. There is typically a large covariance between κ and n. A wide set of bath temperatures allows this degeneracy to be broken for the AdvACT array validation. For example, for ACTPol we could only determine n within 3%,[21,22] while for AdvACT we can determine it within 0.3%. Measuring P_{sat} over a wider range of bath temperatures allows for a better handling of the degeneracy between κ and n in Eq.(1). To minimize array heating in IVs taken in rapid succession, I-V curves were acquired on only a quarter of the array at a time. We measure P_{sat} between 60 and 160 mK every 10 mK, and fit for T_c, κ, and n for each detector. We assume uniform uncertainty for the P_{sat} values and minimize the square of the residuals from Eq.(1) using Powell's method with the SciPy[23] minimization routine. The fitted κ and n values are sensitive to the initial input points, and hence we iteratively solve for the initial points to yield fitted parameters with the smallest residuals.

At 100 mK, the typical operating bath temperature, we target P_{sat} to be 12.5 pW for 150 GHz and 25 pW for 230 GHz. The target parameters are optimized by considering the optical efficiency of the detectors and the potential sources of optical loadings from both instrument and atmosphere. The estimated P_{sat}, T_c, and G are shown in histograms in Figure 3. For the saturation power, we get 12.5 pW is $\pm$ 1 pW for the 150 GHz band and 26 $\pm$ 1pW for the 230 GHz band. P_{sat} is 13 $\pm$ 1 pW for the 150 GHz band and 26 $\pm$ 1pW for the 230 GHz band, within 4-8% of our original targets. After deployment, we checked the detectors are not saturated on the telescope given typical loading levels. Figure 4 shows histogram of the bias power, $P_{bias} = I_{TES} * V_{TES}$, on the TESs under typical observing conditions, and the bias power decreases as the loading gets higher. Thus it is important to understand the loading in the field well in order to set the target parameters of the detectors. The details of various loading estimates are discussed in Section 3.2. The benefits of AlMn are seen in the excellent uniformity of the parameter in Figure 3. Over a full 150 mm wafer, the parameters are 4% in precision and 8% in accuracy; while in ACTPol, we fabricated the detectors on a 3″ wafer and the accuracy ranged from 5-30% in different fabrication runs. Figure 3 also shows the parameters as a function of radial distance from the wafer center, showing a trend in all parameters and T_c in particular. Evidence suggests that this trend is related to the thermal connections between the wafer and the 100 mK support ring. The detector clamp ring design (3) in Figure 1 most likely exerts more uniform pressure within the 20 mm ring radius, and thus we think the discontinuity at 20 mm is the result of the array having a better thermal link to the bath within that radius. For MF arrays, we modify the clamp to have more even mechanical and thermal contact between the mixing chamber stage and the detector array.

Figure 5 shows the bias point of the array where we bias the detectors on its transition during various loading conditions. We target at bias point=0.5, which is 50% of a TES transition. While observation, since the weather condition varies, it is critical to be able to bias the detectors at the targeted bias point, which affects the functionality of detectors, i.e. time response (see Section 3.3) and stability.

3.2 Loading

Minimizing the loading on the detectors is critical to optimize the detector sensitivity, i.e. less total loading means less photon noise, thus higher sensitivity. The loading on the detectors is dominated by the emission from the atmosphere and the optics elements on the telescope. Excess loading can also cause detectors to saturate

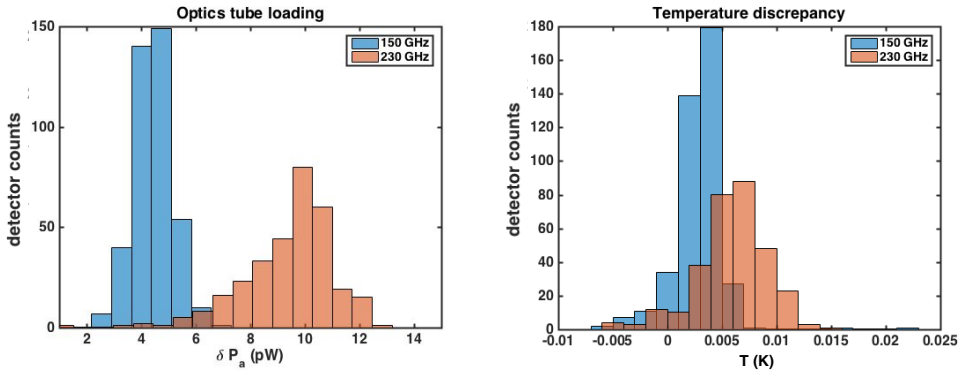

Figure 7: (Left) Histogram of fitted values for extra loading from the optics tube and the 300 K metallic cover used in the field to confirm detector parameters. See Section 3.2 for more details. (Right) Histogram of temperature discrepancy between the thermometer location and the array package, indicating $\lesssim$ 15 mK.

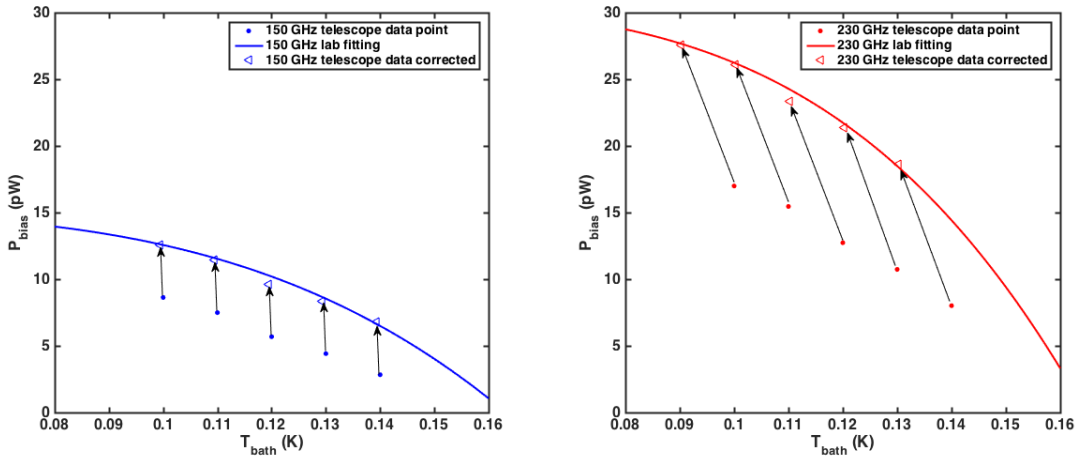

Figure 8: Comparison of I-V curve data taken on the telescope with a metallic cover at 300 K outside the cryostat window to dark laboratory data. P_{bias}s shown here are at 90% Rn. (Left) The 150 GHz data measured on the telescope are shown in filled circles. The triangle points are the corrections to the data using the laboratory fit parameters. The line is the fit to Eq.(1) applying the laboratory κ, n, T_c. Arrows show the shifts in loading and temperature. (Right) Similar data for 230 GHz.

3.3 Time Constants and Array Sensitivity

Measuring the detector time constants is critical to account for its low-pass filter effects on the detector response at high frequencies as the telescope scans. The scan strategy affects the suppression level of the time stream data for a given time constant, hence, we require similar intrinsic time constants between the two frequencies, despite differences in loading which would cause the effective time constants to be different. The time constant is defined as the time, τ, that a detector response takes to reach $1/e$ of its original value after power is added. In the frequency domain, the response is described by $f_{3dB} = \frac{1}{2\pi\tau}$. The intrinsic thermal time constant is defined as

$$\hat{f}_{3dB} = \frac{G}{2\pi C}, \tag{7}$$

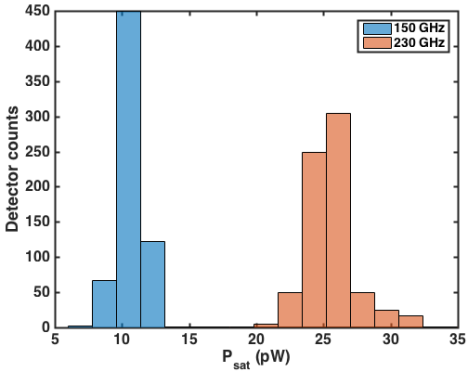

(a) Histogram of saturation powers (90%R_n) at 100 mK.

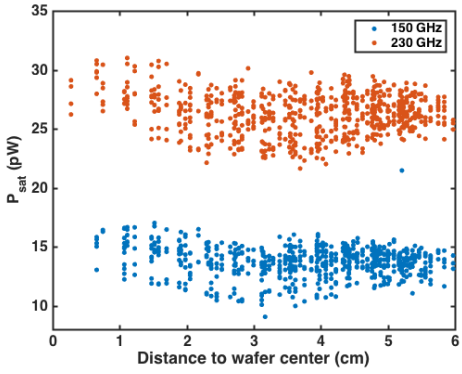

(b) Plot of saturation powers (90%R_n) versus distance to the center of the array.

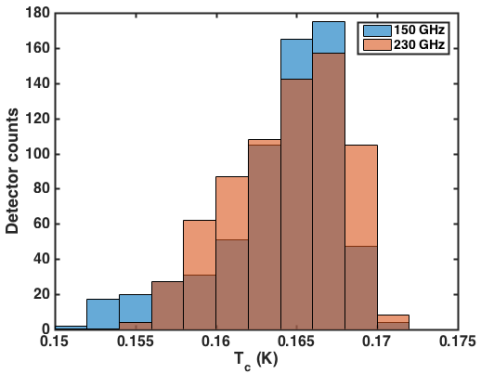

(c) Histogram of critical temperatures.

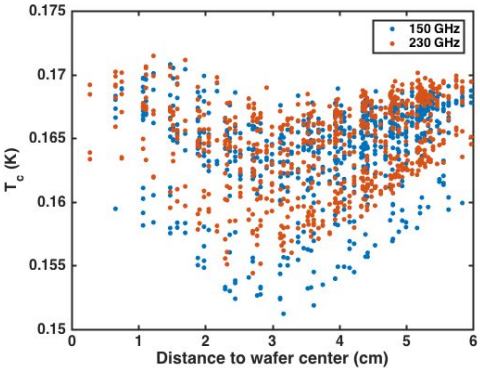

(d) Plot of critical temperature versus distance to the center of the array.

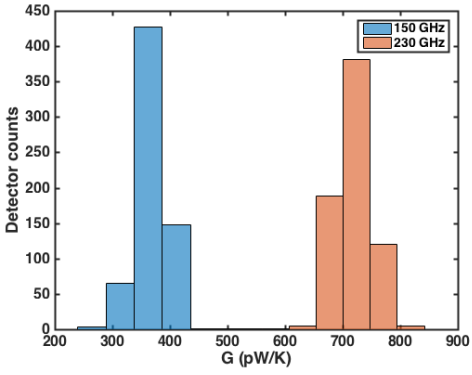

(e) Histogram of thermal conductivities.

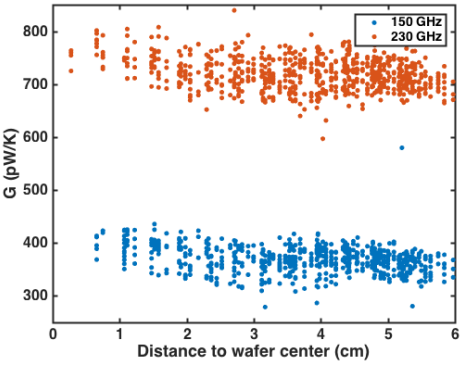

(f) Plot of thermal conductivity versus distance to the center of the array.

Figure 3: TES parameters: histograms and trends versus distance to the center of the array, measured dark in the laboratory before deployment. The wafer shows good uniformity within its 150 mm diameter. The dips in the trend plots around 20 mm away from the center of the wafer are likely related to the wafer heat sinking to the bath. Details are discussed in Section 3.1.

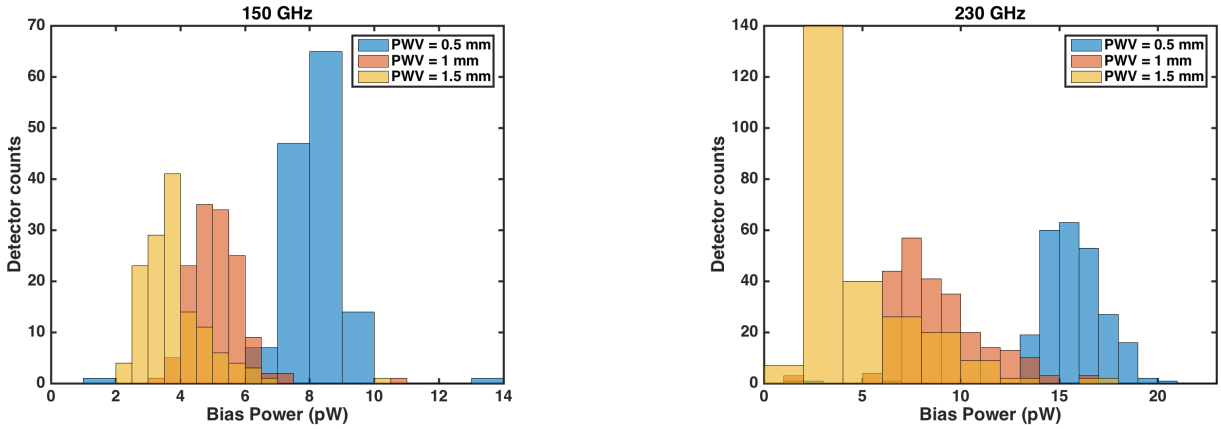

Figure 4: The bias power dissipated in the HF TESs in the field varying with the precipitable water vapor.

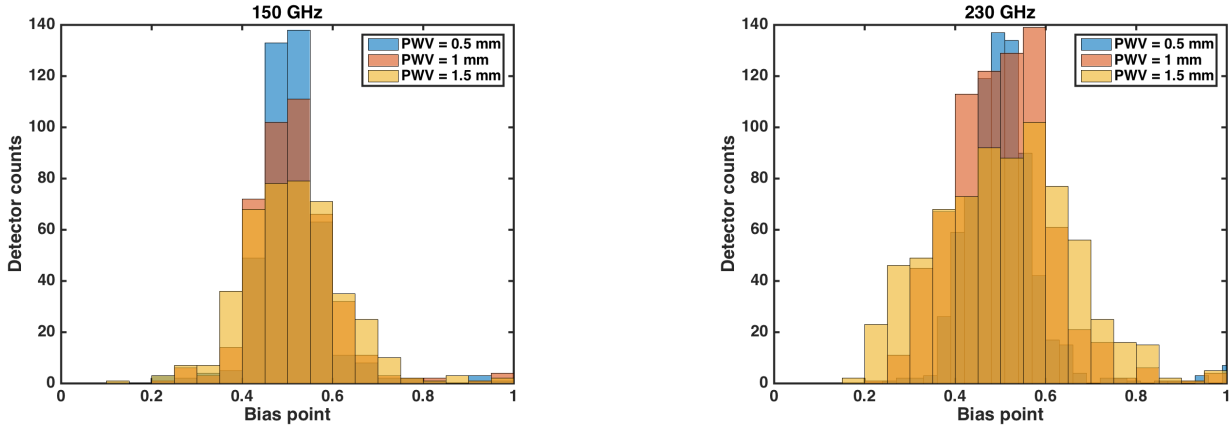

Figure 5: The bias point of HF TESs in the field varying with the precipitable water vapor.

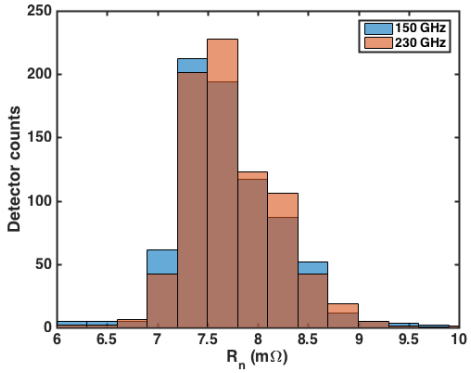

Figure 6: The normal resistance (R_n) of the 150 GHz and 230 GHZ detectors. $< Rn >_{150\ \mathrm{GHz}} = 7.6m\Omega \pm 0.7m\Omega$; $< Rn >_{230\ \mathrm{GHz}} = 7.7 \pm 0.7m\Omega$

.

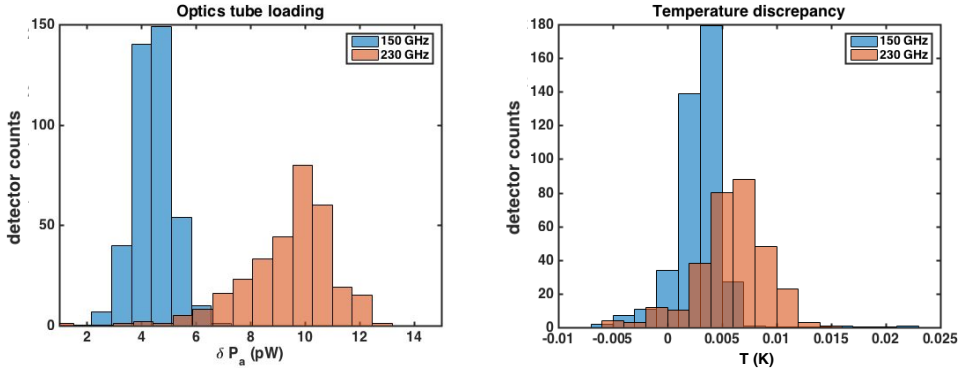

Figure 7: (Left) Histogram of fitted values for extra loading from the optics tube and the 300 K metallic cover used in the field to confirm detector parameters. See Section 3.2 for more details. (Right) Histogram of temperature discrepancy between the thermometer location and the array package, indicating $\lesssim$ 15 mK.

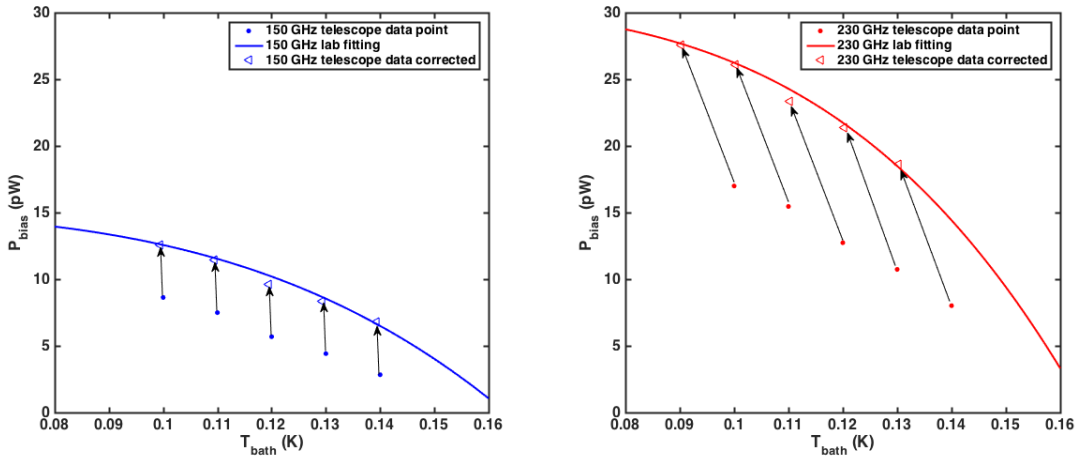

Figure 8: Comparison of I-V curve data taken on the telescope with a metallic cover at 300 K outside the cryostat window to dark laboratory data. P_{bias}s shown here are at 90% Rn. (Left) The 150 GHz data measured on the telescope are shown in filled circles. The triangle points are the corrections to the data using the laboratory fit parameters. The line is the fit to Eq.(1) applying the laboratory κ, n, T_c. Arrows show the shifts in loading and temperature. (Right) Similar data for 230 GHz.

3.3 Time Constants and Array Sensitivity

Measuring the detector time constants is critical to account for its low-pass filter effects on the detector response at high frequencies as the telescope scans. The scan strategy affects the suppression level of the time stream data for a given time constant, hence, we require similar intrinsic time constants between the two frequencies, despite differences in loading which would cause the effective time constants to be different. The time constant is defined as the time, τ, that a detector response takes to reach $1/e$ of its original value after power is added. In the frequency domain, the response is described by $f_{3dB} = \frac{1}{2\pi\tau}$. The intrinsic thermal time constant is defined as

$$\hat{f}_{3dB} = \frac{G}{2\pi C}, \tag{7}$$

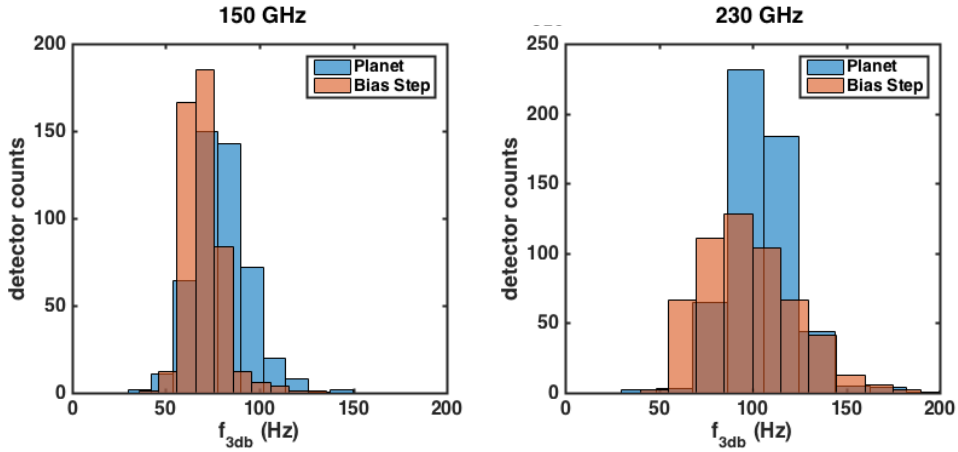

Figure 10: Histograms of f_{3dB}s of 150 GHz (left) and 230 GHz (right) detectors measured by the planet method and the bias step method. The planet scans are taken $\approx$ 20 seconds after bias steps. The planet f_{3dB}s are faster.

optical loading. For Figure. 11, for example, we fit a line for each detector to the f_{3dB} values from the planet method to the bias step method. Then, we apply the fitted coefficient to all the bias step f_{3dB}s as a calibration to correct them to agree with the planet values.

The detector noise is typically defined as Noise Equivalent Power (NEP), which we convert to a thermal value ($\mathrm{NET_{CMB}}$) to describe sensitivity and fluctuations in the CMB thermal blackbody. The detectors are dominated by photon shot noise, and we obtain estimates for the detector noise by Fourier-transforming a time stream to find the white noise floor value at 20 Hz, and converting to Kelvin units with the response to a planet, whose temperature is known, and then correct the Rayleigh Jeans estimate NET to $\mathrm{NET_{CMB}}$. When the PWV is around 0.5 mm, the total array sensitivity is 11 $\mu K\sqrt{\mathrm{s}}$ in the 150 GHz band and 21 $\mu K\sqrt{\mathrm{s}}$ in the 230 GHz band, estimated from maps after data selection.

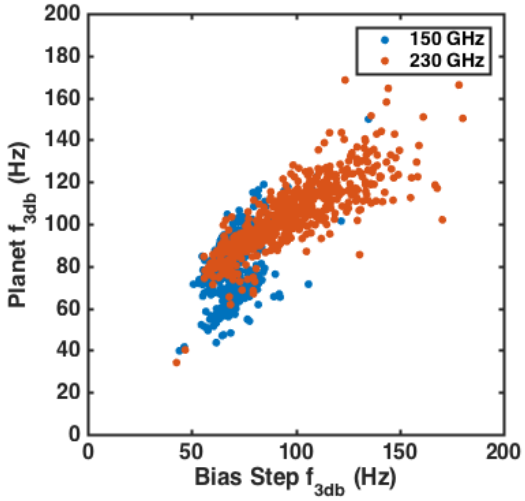

Figure 11: Scatter plot of mean f_{3dB} measurements from the planet method and the bias step method. In the figure, each data point is the average of the time ordered data collection from eight files of separate Uranus observations.

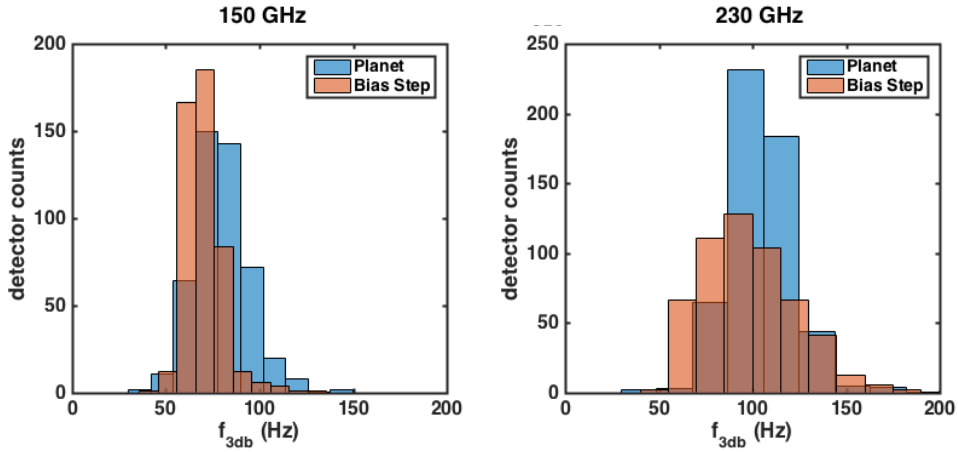

Figure 10: Histograms of f_{3dB}s of 150 GHz (left) and 230 GHz (right) detectors measured by the planet method and the bias step method. The planet scans are taken $\approx$ 20 seconds after bias steps. The planet f_{3dB}s are faster.

optical loading. For Figure. 11, for example, we fit a line for each detector to the f_{3dB} values from the planet method to the bias step method. Then, we apply the fitted coefficient to all the bias step f_{3dB}s as a calibration to correct them to agree with the planet values.

The detector noise is typically defined as Noise Equivalent Power (NEP), which we convert to a thermal value ($\mathrm{NET_{CMB}}$) to describe sensitivity and fluctuations in the CMB thermal blackbody. The detectors are dominated by photon shot noise, and we obtain estimates for the detector noise by Fourier-transforming a time stream to find the white noise floor value at 20 Hz, and converting to Kelvin units with the response to a planet, whose temperature is known, and then correct the Rayleigh Jeans estimate NET to $\mathrm{NET_{CMB}}$. When the PWV is around 0.5 mm, the total array sensitivity is 11 $\mu K\sqrt{\mathrm{s}}$ in the 150 GHz band and 21 $\mu K\sqrt{\mathrm{s}}$ in the 230 GHz band, estimated from maps after data selection.

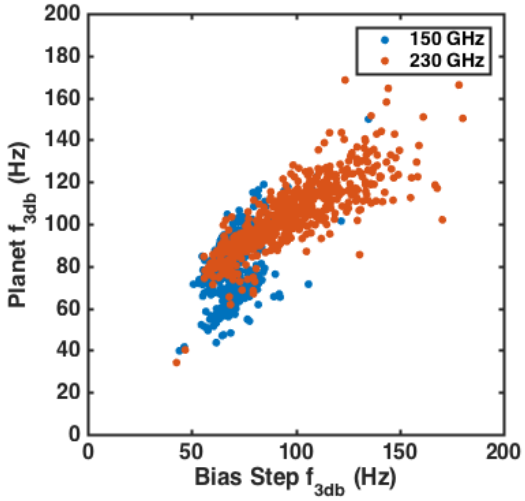

Figure 11: Scatter plot of mean f_{3dB} measurements from the planet method and the bias step method. In the figure, each data point is the average of the time ordered data collection from eight files of separate Uranus observations.

which is tuned by the added region of PdAu on the island. Different from ACTPol, we chose to adjust the geometry of PdAu on the TES island as opposed to the thickness so that the PdAu could be put down in just one layer without the need for additional masks.

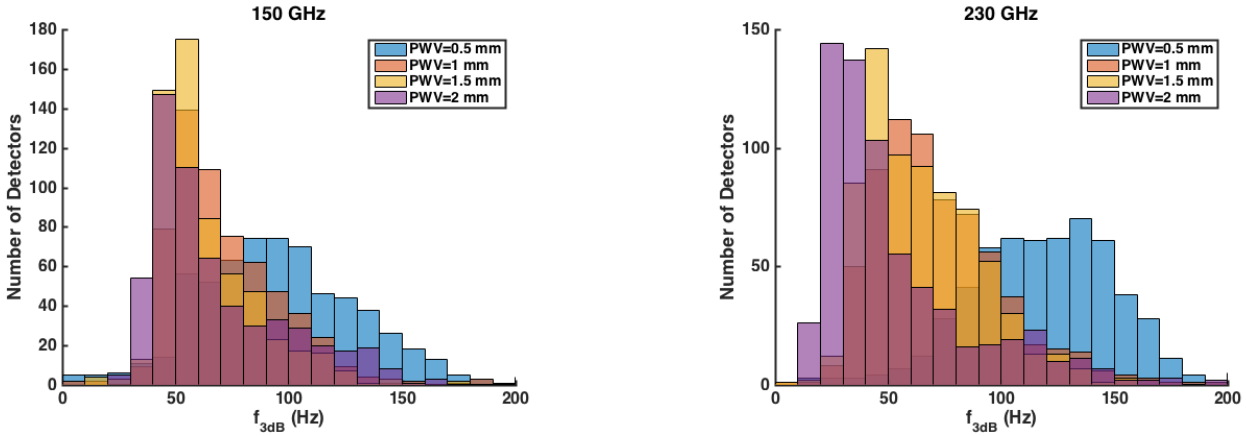

Figure 9: The time constant histograms plotted in different loading conditions, which make the bias powers different, thus make the f_{3dB}s vary from time to time (in Equation 7).

During observation, the f_{3dB} varies with the operating conditions (P_{bias}) of the TES:[20]

$$f_{3dB} = \frac{1}{2\pi}\left(\frac{1}{\tau} + \frac{\alpha}{(1+\beta)}\frac{1}{T_c\, C}P_{bias}\right), \tag{8}$$

where α and β are the logarithmic derivatives of the TES resistance with respect to temperature and current, respectively (Figure 9).

Thus f_{3dB} must be measured in the field at frequent intervals. We use two methods for measuring the temporal response of the TES bolometers: the planet observation method and the bias step method. The former can be found by scanning back and forth over a planet (we use Uranus because it doesn't saturate), because a finite response time causes the peak position to shift in opposite directions for backwards and forwards going scans. The change in peak position can be used to derive the time constant associated with optical loading, which is relevant for CMB observations. Planet measurement is a more direct probe of the optical response; however, this scan cannot be performed very frequently. To track the different loadings from time to time (from atmosphere and other effects), and update the time constants per scan, we perform the bias step method. We take bias step measurements of the detectors every $\sim$10 minutes. Each takes about $\sim$ 10 seconds. The bias step method consists of driving the detector bias with a small square wave on top of a DC level, which is the nominal TES bias point, and measuring the time constant of the detector response.[21] We fit the rising and falling slopes of bias step response to an exponential plus a constant:

$$f(t) = A\exp^{-t/\tau} + B \tag{9}$$

The histograms of f_{3dB} from the planet and bias step methods are shown in Figure 10. Both planet histograms are plotted from an average of eight nighttime planet observations in weather conditions with PWV $\approx$ 0.5 mm.

The optical time constants from the planet method are measured to be faster than those from the bias step method. This is because the TESs are coupled differently to the photon power loading than the electrical power loading.[25] The measurements of f_{3dB} from the planet method are larger than from the bias step method, which implies that the absorber is coupled to the silicon more strongly than the TES to the silicon. To account for this difference between the two methods, we fit a line to planet and bias step measurements performed at the same time, and use the slope and intercept to correct the more frequent bias step methods to the values relevant for

R. Thornton, H. Trac, J. Treu, C. Tucker, A. V. Engelen, J. T. Ward, and E. J. Wollack, "The Atacama Cosmology Telescope: Two-Season ACTPol Spectrum and Parameters," 2016.

5. S. Henderson, R. Allison, J. Austermann, T. Baildon, N. Battaglia, J. Beall, D. Becker, F. D. Bernardis, J. Bond, E. Calabrese, S. Choi, K. Coughlin, K. Crowley, R. Datta, M. Devlin, S. Duff, R. Dunner, J. Dunkley, A. van Engelen, P. Gallardo, E. Grace, M. Hasselfield, F. Hills, G. Hilton, A. Hincks, R. Hlozek, S. Ho, J. Hubmayr, K. Huffenberger, J. Hughes, K. Irwin, B. Koopman, A. Kosowsky, D. Li, J. McMahon, C. Munson, F. Nati, L. Newburgh, M. Niemack, P. Niraula, L. Page, C. Pappas, M. Salatino, A. Schillaci, B. Schmitt, N. Sehgal, B. Sherwin, J. Sievers, S. Simon, S. Staggs, J. Stevens, R. Thornton, J. V. Lanen, E. Vavagiakis, J. Ward, and E. Wollack, "Advanced ACTPol cryogenic detector arrays and readout," Journal of Low Temperature Physics, 2015.
6. F. D. Bernardis, J. R. Stevens, D. A. M. Hasselfieldb, c, J. R. Bond, E. Calabrese, S. K. Choi, K. T. Crowley, M. Devlin, J. Dunkley, P. A. Gallardo, S. W. Henderson, M. Hilton, R. Hlozek, S. P. Ho, K. Huffenberger, B. J. Koopman, A. Kosowsky, T. Louis, M. S. Madhavacheril, J. McMahon, S. Naess, F. Nati, L. Newburgh, M. D. Niemack, L. A. Page, M. Salatino, A. Schillaci, B. L. Schmitt, N. Sehgal, J. L. Sievers, S. M. Simon, D. N. Spergel, S. T. Staggs, A. van Engelene, E. M. Vavagiakis, and E. J. Wollack, "Survey strategy optimization for the Atacama Cosmology Telescope," 2016.
7. S. Duff, J. Austermann, J. Beall, D. Becker, R. Datta, P. Gallardo, S. Henderson, G. Hilton, S. Ho, J. Hubmayr, B. Koopman, D. Li, J. McMahon, F. Nati, M. Niemack, C. Pappas, M. Salatino, B. Schmitt, S. Simon, S. Staggs, J. Stevens, J. V. Lanen, E. Vavagiakis, J. Ward, and E. Wollack, "Advanced ACTPol multichroic polarimeter array fabrication process for 150 mm wafers," Journal of Low Temperature Physics, 2015.
8. J. T. Ward, J. A. Beall, S. K. Choi, K. T. Crowley, M. J. Devlin, S. M. Duff, P. M. Gallardo, S. W. Henderson, S.-P. P. Ho, J. Hubmayr, N. Khavari, B. J. Koopman, D. Li, G. Mumby, F. Nati, M. D. Niemack, M. Salatino, A. Schillaci, B. L. Schmitt, S. M. Simon, S. T. Staggs, R. Thornton, J. N. Ullomb, and E. M. Vavagiakis, "Mechanical design and development of tes bolometer detector arrays for the Advanced ACTPol experiment," Proc. SPIE, 2016.
9. K. Coughlin, "Silicon metamaterial optical elements for measurement of the cosmic microwave background." SPIE poster, 2016.
10. R. Datta, J. Austermann, J. Beall, D. Becker, K. P. Coughlin, S. Duff, P. Gallardo, E. Grace, M. Hasselfield, S. Henderson, G. Hilton, S. Ho, J. Hubmayr, B. Koopman, J. Lanen, D. Li, J. McMahon, C. Munson, F. Nati, M. Niemack, L. Page, C. Pappa, M. Salatino, B. Schmitt, A. Schillaci, S. Simnon, S. Staggs, J. Stevens, E. Vavagiakis, J. Ward, and E. Wollack, "Design and deployment of a multichroic polarimeter array on the Atacama Cosmology Telescope," Journal of Low Temperature Physics, 2015.
11. D. Li, J. E. Austermann, J. A. Beall, D. T. Becker, S. M. Duff, P. A. Gallardo, S. W. Henderson, G. C. Hilton, S.-P. Ho, J. Hubmayr, B. J. Koopman, J. J. McMahon, F. Nati, M. D. Niemack, C. G. Pappas, M. Salatino, B. L. Schmitt, S. M. Simon, S. T. Staggs, J. V. Lanen, J. T. Ward, and E. J. Wollack, "AlMn transition edge sensors for Advanced ACTPol," Journal of Low Temperature Physics, 2015.
12. C. G. Pappas, J. Austermann, S. M. D. J. A. Beall, P. A. Gallardo, E. Grace, S, W. Henderson, S. Ho, B. J. Koopman, D. Li, J. McMahon, F. Nati, M. D. Niemack, M. S. P. Niraula, A. Schillaci, B. L. Schmitt, S. M. Simon, S. Staggs, J. R. Stevens, E. M. Vavagiakis, J. T. Ward, and E. J. Wollack, "High-density superconducting cables for Advanced ACTPol," Journal of Low Temperature Physics, 2015.
13. J. A. Chervenak, K. D. Irwin, E. N. Grossman, J. M. Martinis, C. D. Reintsema, and M. E. Huber, "Superconducting multiplexer for arrays of transition edge sensors," Applied Physics Letter, 1999.
14. W. B. Doriese, K. M. Morgan, D. A. Bennett, E. V. Denison, C. P. Fitzgerald, J. W. Fowler, J. D. Gard, J. P. Hays-Wehle, G. C. Hilton, K. D. Irwin, Y. I. Joe, J. A. B. Mates, G. C. O'Neil, C. D. Reintsema, N. O. Robbins, D. R. Schmidt, D. S. Swetz, H. Tatsuno, L. R. Vale, and J. N. Ullom, "Developments in time-division multiplexing of x-ray transition-edge sensors," **184**(1), pp. 389–395, Journal of Low Temperature Physics, 2016.
15. S. W. Henderson, J. R. Stevens, M. Amiri, J. Austermann, J. A. Beall, S. Chaudhuri, H.-M. Cho, S. K. Choi, N. F. Cothard, K. T. Crowley, S. M. Duff, C. P. Fitzgerald, P. A. Gallardo, M. Halpern, M. Hasselfield, G. Hilton, S.-P. P. Ho, J. Hubmayr, K. D. Irwin, B. J. Koopman, D. Li, J. McMahon, F. Nati, M. D. Niemack, C. D. Reintsema, M. Salatino, A. Schillaci, B. L. Schmitt, S. M. Simond, S. T. Staggs, E. M.

Vavagiakisa, and J. T. Ward, "Readout of two-kilopixel transition-edge sensor arrays for Advanced ACTPol," Proc. SPIE, 2016.
16. Y. Li, S. Choi, S.-P. Ho, K. T.Crowley, M. Salatino, S. M. Simon, S. T. Staggs, F. Nati, B. L. Schmitt, S. Henderson, B. J. Koopman, P. A. Gallardo, E. M. Vavagiakis, M. D. Niemack, J. McMahon, S. M. Duff, and A. Schillaci, "Assembly and integration process of the first high density detector array for the Atacama Cosmology Telescope," Proc. SPIE, 2016.
17. E. M. George, J. E. Austermann, J. A. Beall, D. Becker, B. A. Benson, L. E. Bleem, J. E. Carlstrom, C. L. Chang, H.-M. Cho, A. T. Crites, M. A. Dobbs, W. Everett, N. W. Halverson, J. W. Henning, G. C. Hilton, W. L. Holzapfel, J. Hubmayr, K. D. Irwin, D. Li, M. Lueker, J. J. McMahon, J. Mehl, J. Montgomery, T. Natoli, J. P. Nibarger, M. D. Niemack, V. Novosad, J. E. Ruhl, J. T. Sayre, E. Shirokoff, K. T. Story, G. Wang, V. Yefremenko, K. W. Yoon, and E. Young, "A study of Al-Mn transition edge sensor engineering for stability," Journal of Low Temperature Physics, 2013.
18. E. Grace, J. Beall, J. Britton, H. Cho, M. Devlin, A. Fox, G. Hilton, J. Hubmayr, K. Irwin, J. Klein, M. Lungu, L. Newburgh, J. Nibarger, M. Niemack, J. McMahon, L. Page, C. Pappas, B. Schmitt, S. Staggs, and E. Wollack, "Design and performance of kilo-pixel TES arrays for ACTPol," Applied Superconductivity, 2013.
19. T. Essinger-Hileman, J. Appel, J. Beall, H. Cho, J. Fowler, M. Halpern, M. Hasselfield, K. Irwin, T. Marriage, M. Niemack, L. Page, L. Parker, S. Pufu, S. Staggs, O. Stryzak, C. Visnjic, K. W. Yoon, and Y. Zhao, "The Atacama B-mode Search: CMB polarimetry withTransition-Edge-Sensor bolometers," Journal of Low Temperature Physics, 2013.
20. K. D. Irwin and G. C. Hilton, *Transition-Edge Sensors*, vol. 99 of *Topics Appl. Phys.*, Springer-Verlag Berlin Heidelberg, 2005.
21. E. Grace, *Detector Characterization, Optimization, and Operation for ACTPol.* PhD thesis, Princeton University, 2015.
22. C. G. Pappas, *Assembly, characterization, and operation of large-scale TES detector arrays for ACTPol.* PhD thesis, Princeton University, 2015.
23. E. Jones, T. Oliphant, P. Peterson, *et al.*, "SciPy: Open source scientific tools for Python," 2001–. [Online; accessed ¡today¿].
24. K. T. Crowley and S. K. C. et.al., "Data-driven electrothermal and noise modeling of tes detectors in multichroic arrays for Advanced ACTPol," Proc. SPIE, 2016.
25. J. Appel, "Determining the time constants of ACT's TES bolometers." Experimental Project, 2007.